# A three-phase flow simulation of local scour caused by a submerged wall jet with a water-air interface

Cheng-Hsien Lee[a], Conghao Xu[b], Zhenhua Huang[b,*]

[a]*Department of Water Resources and Environmental Engineering, Tamkang University, Taiwan*
[b]*Department of Ocean and Resources Engineering, School of Ocean and Earth Science and Technology, University of Hawaii at Manoa, Honolulu HI 96822, USA*

**Abstract**

Interactions between fluid and hydraulic structures and the resulting bed scouring are complex phenomena that involve three phases: water, air and sediment. This study presents a new rheology-based three-phase model that can capture the water-air interface in the presence of suspended sediment and simulate the bed scouring process. A modified volume-of-fluid (VOF) method was used to track the water-air interface, and a modified k-$\epsilon$ turbulence model was employed to capture important features of the turbulent flow, including turbulence modulation due to fluid-sediment interaction. The three-phase model was first used to study the sediment transport in open-channel flows in order to evaluate the performance of two models for particle response time. The three-phase model was then employed to simulate the scouring process downstream a submerged wall jet issued from a sluice gate. The simulated bed profiles showed good agreement with the measured. It was demonstrated that the three-phase model could capture important dynamic features such as sediment avalanche.

*Keywords:* Three-phase modeling; Volume of fluid; Sediment transport; Scour process; Sediment avalanche

## 1. Introduction

The movement of sediment gains due to fluid flow surrounding them is a two-phase phenomena in nature, where the fluid is the carrier phase and the sediment is the dispersed phase. Understanding sediment transport is important in hydraulic and coastal engineering. When a flow passes a hydraulic structure, the flow pattern changes due to the obstruction of the flow and the formation of vortices, causing the local sediment transport rate to increase. The increased sediment transport rate usually leads to scouring, which can pose a threat to the stability of the structure [1]. To better understand

*Corresponding author contacts:
*Email address:* zhenhua@hawaii.edu (Zhenhua Huang)

scouring process, numerical models dedicated to modeling sediment-laden flows and the resulting scour are necessary tools in addition to physical model tests.

At present, most of numerical models have been developed for this purpose are single-phase models, treating the sediment as a passive scalar with a falling velocity but ignoring effects of particles on the flow and particle-particle interactions [2, 3, 4, 5]. The sediment transport in these models is classified into two modes: the suspended load mode and the bed load mode. The bed-load transport rate is computed using empirical or semi-empirical formulas, such as the formula proposed by Engelund and Fredsøe [6], who obtained the mean sediment velocity by simply considering the average equilibrium of the drag and friction forces exerted on a single particle and assuming the flow velocity around the particle to be a simple linear function of shear velocity. However, the flow in the bed-load layer is complex, and the effects of fluid-particle and particle-particle interactions can be important and should be considered in the simulation [7].

Important fluid-particle interactions include the turbulence modulation by sediment [8] and the momentum interchange between the sediment and the fluid [9], both of which can change the flow field and sediment transport. The particle-particle interaction is responsible for the rheological characteristics of the fluid-sediment mixture. The effects of enduring contact and mutual collision as well as fluid viscous effects [10, 11] all can affect the particle-particle interaction: the enduring-contact effect leads to the Coulomb relationship [10]; the inertial effect has to do with the stresses that depend on the square of the strain rates [12]; and the viscous effects yield the stresses that are associated with the strain rates [12]. The enduring-contact effect is important only for very high concentration flows. The particle size and shear velocity determines the relative importance of inertial and fluid viscous effects: in flows with high shear velocity and large particles, the inertial effect dominates; in flows with low shear velocity and small particles, the fluid viscous effect dominates.

Some models have been developed in the two-phase framework [13, 14, 15, 16, 17, 18, 19] to consider the coupled fluid-particle and particle-particle interactions. In two-phase flow models, both the sediment and fluid phases have their own governing equations for mass and momentum. The momentum equations take into account of the drag force between the two phases and the turbulent dispersion effect. Early two-phase flow models considered the turbulence modulation by simply reducing the mixing length according to concentration [13]; more sophisticated two-phase models included additional terms describing the turbulence modulation in two-equation turbulence models [14], which consider two effects: (1) the dissipation of turbulence due to the correlation between the fluctuating velocities of sediment and fluid phases; (2) the buoyancy production of turbulence due to the gradient in sediment concentration. Because solving the equations governing multi-dimensional two-phase flow problems in early days was not permitted by the computers at the time, most of

the numerical studies using two-phase flow models were confined to 1D problems. Even though few studies [15, 16] did two-dimensional two-phase flow simulations, the bed location (the interface between the static sand layer and the mobile layer) must be specified at each time step during the computation. Recently, some authors [19, 20] used the open source package OpenFOAM [21] to develop multi-dimensional two-phase flow models, eliminating the needs for specifying bed location, and some favorable preliminary results have been obtained using these two-phase flow models.

Flows passing through hydraulic structures may change the water-air interface, which in turn influences the flow field and sediment transport [22]. It is necessary to consider the water-air interface when simulating scour. Bakhtyar et al. [23] developed a three-phase (air, water, and sediment) model which can capture the water-air interface in the presence of sediment; however, their model included only the viscous effects on sediment stresses and the effects of buoyancy production on turbulence modulation.

This study will develop a three-phase model by introducing a third phase for air into the liquid-solid two-phase model of Lee et al. [19]. which considered enduring contact, mutual collision (inertial), fluid viscous effects in sediment stress, and two mechanisms of turbulence modulation. For model verification, the three-phase model is applied to simulate the local scour caused by a submerged wall jet with a water-air surface, a phenomenon commonly encountered in sluice-gate problems and having applications in hydroelectric power plants and irrigation.

## 2. Mathematical formulation

The governing equations for three-phase flows (air, water and sediment) and the related closures are presented in this section. Two models for particle response time, $\tau_p$, which is used to compute the drag force, are examined: one is based on sedimentation [24] and the other is based on the pressure drop in steady flow through a porous media [6].

### *2.1. Governing equations*

A volume-of-fluid (VOF) method [25] is used to track the water-air interface. In VOF methods, the air-water interface is defined as a region occupied by a mixture of water and air. Liquid saturation $s$ is defined as the ratio of the volume of water to the total volume of void (air and water) in a control volume. Liquid saturation is used as an indicator function for classifying whether a spatial point is occupied by air, water or both. For $s = 1$, the region is occupied by water alone; for $s = 0$, the region is occupied by air alone; for $0 < s < 1$, the region is defined as the water-air interface. In the absence of the sediment phase, the indicator function for three-phase flows should reduce to that used for liquid-gas flows [26].

To determine the water-air interface, we consider the water and air phases as a single fluid phase of water-air mixture with a variable density and a variable viscosity. As in previous studies on liquid-gas flows [26], the density, $\rho_f$, and viscosity, $\nu_f$, of the fluid phase (the water-air mixture) are determined by

$$\rho_f = s\rho_w + (1-s)\rho_a, \tag{1}$$

and

$$\nu_f = s\nu_w + (1-s)\nu_a, \tag{2}$$

where $\rho_w$ and $\rho_a$ are the densities of the water and air phases, respectively; $\nu_w$ and $\nu_a$ are the kinematic viscosities of the water and air phases, respectively. The velocities of the water and air phases are assumed to be the same at the water-air interface due to the no-slip condition.

The mass-balance equations for three-phase flows can be obtained through averaging processes [27], and they can be written as [27]:

$$\frac{\partial c}{\partial t} + \nabla \cdot [c\mathbf{u}^s] = 0 \tag{3}$$

for the sediment phase,

$$\frac{\partial (1-c)s}{\partial t} + \nabla \cdot \left[(1-c)s\mathbf{u}^f\right] = 0 \tag{4}$$

for the liquid phase, and

$$\frac{\partial (1-c)(1-s)}{\partial t} + \nabla \cdot \left[(1-c)(1-s)\mathbf{u}^f\right] = 0 \tag{5}$$

for the gaseous phase.

Since the flow beneath the water-air interface is a solid-liquid two-phase flow, the equations for momentum balance are the same as those used in the previous two-phase models [14, 19]:

$$\begin{aligned}\frac{\partial \rho_s c\mathbf{u}^s}{\partial t} + \nabla \cdot [\rho_s c\mathbf{u}^s\mathbf{u}^s] =& \rho_s cg - c\nabla p_f - \nabla(cp_s) + \nabla \cdot [c\mathbf{T}^s] \\ &+ c\rho_s \frac{(\mathbf{u}^f - \mathbf{u}^s)}{\tau_p} - \frac{\rho_s}{\tau_p}\frac{(1-c)\nu_{ft}}{\sigma_c}\nabla c\end{aligned} \tag{6}$$

for the sediment phase, and

$$\begin{aligned}\frac{\partial \rho_f (1-c)\mathbf{u}^f}{\partial t} + \nabla \cdot [\rho_f (1-c)\mathbf{u}^f\mathbf{u}^f] =& \rho_f (1-c)g - (1-c)\nabla p_f + \nabla \cdot \left[(1-c)\mathbf{T}^f\right] \\ &- c\rho_s \frac{\mathbf{u}^f - \mathbf{u}^s}{\tau_p} + \frac{\rho_s}{\tau_p}\frac{(1-c)\nu_{ft}}{\sigma_c}\nabla c\end{aligned} \tag{7}$$

for the liquid phase. In Eqs. (6) and (7), $s$ and $f$, which are either subscripts or the superscripts, refer to the fluid and solid phases, respectively; $\rho$ = the density; $c$ = the volume concentration of sediment; $\mathbf{u}$ = the velocity; $\mathbf{g}$ = the gravitational acceleration; $p$ = pressure; $\mathbf{T}$ = stress tensor;

$\tau_p$ = the particle response time; $\nu_{ft}$ = the eddy viscosity of the liquid phase; $\sigma_c$ = the Schmidt number. The last two terms in Eqs. (6) and (7) are related to momentum interchanges between the solid and liquid phases: the first term accounts for the drag force and the second term for turbulent dispersion.

A $k-\epsilon$ model with a low-Reynolds-number correction is applied to compute $\mathbf{T}^f$ [19]. The turbulence kinetic energy, $k$, and its dissipation rate, $\epsilon$, are governed by

$$\begin{aligned}\frac{\partial \rho_f(1-c)k}{\partial t} + \nabla\cdot[\rho_f(1-c)\mathbf{u}^f k] &= (1-c)\mathbf{T}^f : \nabla\mathbf{u}^f - \rho_f(1-c)\epsilon \\ &+ \nabla\cdot[\rho_f\frac{\nu_{ft}}{\sigma_k}(1-c)k] \\ &- \left\{(\rho_s-\rho_f)\frac{(1-c)\nu_{ft}}{\sigma_c}\nabla c\cdot\mathbf{g} + \frac{2\rho_s c(1-\alpha)k}{\tau_p}\right\}\end{aligned} \tag{8}$$

and

$$\begin{aligned}\frac{\partial \rho_f(1-c)\epsilon}{\partial t} + \nabla[\rho_f(1-c)\mathbf{u}^f\epsilon] &= \frac{\epsilon}{k}[C_{\epsilon1}f_1(1-c)\mathbf{T}^f : \nabla\mathbf{u}^f - C_{\epsilon2}f_2\rho_f(1-c)\epsilon] \\ &+ \nabla\cdot\left[\rho_f\frac{\nu_{ft}}{\sigma_\epsilon}(1-c)\epsilon\right] \\ &- \frac{\epsilon}{k}C_{\epsilon3}\left\{(\rho_s-\rho_f)\frac{(1-c)\nu_{ft}}{\sigma_c}\nabla c\cdot\mathbf{g} + \frac{2\rho_s c(1-\alpha)k}{\tau_p}\right\},\end{aligned} \tag{9}$$

where $C_{\epsilon1}$, $C_{\epsilon2}$, $\sigma_\epsilon$, $\sigma_k$ , and $f_2$ all are model parameters, with their values being the same as those in $k-\epsilon$ model for clear water. At present, we don't have a good understanding of the model parameter $C_{\epsilon3}$. The parameter $\alpha$ measures how well the particles follow the fluid fluctuation. The two terms in { } in Eqs. (8) and (9) account for the turbulence modulation due to the presence of particles: the first term is associated to buoyancy and the second term is due to the correlation between the fluctuating velocities of sediment and fluid. For other details about the $k-\epsilon$ model used here, the reader is referred to Lee et al. [19].

### *2.2. Sediment stresses*

Lee et al. [19] suggested that $p_s$ and $\mathbf{T}^s$ should consider: (1) the elastic behavior for static compact granular material [14]; (2) the turbulent behavior of sediment motion [28]; and (3) the rheological characteristics of the fluid-particle mixture [29]. Consequently, the pressure of the sediment phase is a superposition of three components

$$p_s = p_{sr} + p_{se} + p_{st}, \tag{10}$$

where $p_{sr}$ reflects the rheological characteristics when the sediment is in motion, $p_{se}$ accounts for the elastic effect when sediment is in its static state, and $p_{st}$ accounts for the turbulent motion of sediment phase.

Lee et al. [19] used a regularization technique that regards the static sediment layer as a very viscous fluid and wrote $\mathbf{T}^s$ as

$$\mathbf{T}^s = -\left(\frac{2}{3}\rho_s\nu_s\nabla\cdot\mathbf{u}^s\right) + 2\rho_s\nu_s\mathbf{D}^s, \tag{11}$$

where $\mathbf{D}^s$ is the strain rate. $\nu_s$ is modeled by

$$\nu_s = \nu_{sv} + \nu_{st}, \tag{12}$$

where $\nu_{sv}$ and $\nu_{st}$ account for the rheological characteristics (visco-plastic effect) and turbulence effects, respectively.

Closures for $p_{sr}, p_{se}, p_{st}, \nu_{sv}$, and $\nu_{st}$ are needed. In the following, we only present the models for $p_{sr}$ and $\nu_{sv}$ for later discussion; for other parameters, the reader is referred to Lee et al. [19].

Bagnold [12] suggested that the rheological characteristics should have two regimes, which can be distinguished by the so-called Bagnold number, $Ba = \rho_s d D^s/\rho_f\nu_f$, where $d$ is the diameter of sediment particles and $D^s = |\mathbf{D}^s|$. In the inertial regime, the value of $Ba$ is large, while in the viscous regimes the value of $Ba$ is small. Bagnold [12] proposed two formulas to compute $\mathbf{T}^s$ in these two regimes by assuming that $|\mathbf{T}^s|/p_s$ is a function of constant $\eta$. In the last decade, some studies find that the constant $\eta$ depends on the inertial number, $I_i = 2dD^s/\sqrt{cp_s/\rho_s}$ for large values of $Ba$ [30], the viscous number $I_v = 2\rho_f\nu_f D^s/cp^s$ for small values of $Ba$ [11], or the combination of the two $I = I_v + aI_i^2$ [29] with $a$ being a constant. The inertial number is the ratio of inertial shear stress to friction shear stress associated with the weight (resulting from enduring contact). The viscous number is the ratio of the viscous shear stress to the friction shear stress, and the value of $a$ depends on the critical value of $Ba$ at which sediment dynamics transfer from one regime to the other. Many models for the relationship between $\eta$ and $I$ have been proposed, and one example is

$$\eta = \eta_1 + \frac{\eta_2 - \eta_1}{1 + I_o/I} \tag{13}$$

with $\eta_1$, $\eta_2$, and $I_o$ being constants [29]. In Eq. (13), $\eta_1$ is associated with the angle of repose. Using the regularization technique, Lee et al. [19] computed $\nu_{sv}$ by

$$\nu_{sv} = \frac{(p_{sr} + p_{se})\eta}{2\rho_s D^s}, \tag{14}$$

where $\eta$ was given by Eq. (14).

Previous studies [11, 29, 30] found that $c$ decreased monotonically from a constant $c_c$ (around 0.6) when $I_i$, $I_v$, or $I$ was increased. Based on these finding, Lee et al. [19] suggested that $p_{sr}$ be computed by

$$p_{sr} = \frac{2b^2c}{(c_c - c)^2}(\rho_f\nu_f + 2a\rho_s d^2 D^s)D^s, \tag{15}$$

where $b$ is a constant.

*2.3. Particle response time*

Particle response time ($\tau_p$), which is related to the drag coefficient, has effects on the momentum interchange between the two phases. At present, there is no universal model available for computing $\tau_p$. Two models for $\tau_p$ will be examined in this study: one model is based on sedimentation [24] (valid for $c < 0.4$ [31]) and the other is based on steady flow through porous media [6] (see also [32]).

The first model examined in this study is based on sedimentation test. The particle response time can be written as

$$\tau_p = \frac{\rho_s}{\rho_f - \rho_s} \frac{w}{(1-c)^2 g}, \tag{16}$$

where $w$ is the hindered settling velocity, the sedimentation velocity of sediment particles in a particle cloud. Richard and Zaki [24] suggested that the hindered settling velocity should be smaller than the terminal settling velocity of a single particle, $w_s$, and proposed the following relationship between $w$ and $w_s$

$$\frac{w}{w_s} = (1-c)^n, \tag{17}$$

where $c$ is the concentration and $n$ is given by

$$n = \begin{cases} 4.65, & Re_s < 0.2 \\ 4.4 Re_s^{-0.33}, & 0.2 \le Re_s < 1 \\ 4.4 Re_s^{-0.1}, & 1 \le Re_s < 500 \\ 2.4, & 500 \le Re_s \end{cases}, \tag{18}$$

where $Re_s = w_s d/\nu_f$ is the particle settling Reynolds number. The terminal velocity of a single particle can be computed by [33]

$$w_s = \sqrt{\frac{4dg}{3C_d} \frac{\rho_s - \rho_f}{\rho_f}}, \tag{19}$$

where $C_d$ is the drag coefficient for steady flows passing a small object. For spheres, White [9] suggested

$$C_d = \frac{24}{Re_p} + \frac{6}{1 + \sqrt{Re_p}} + 0.4, \tag{20}$$

where $Re_p$ is the particle Reynolds number defined by $Re_p = |u^f - u^s| d/\nu_f$. The model for $\tau_p$ based on Eqs. (16)-(20) is referred to as the "RZ" model (i.e., Richard and Zaki model) hereafter.

The second model examined in this study is based on pressure drop when flow pass through porous media. According to the study of Engelund and Fredsøe [6], $\tau_p$ can be computed by

$$\tau_p = \frac{\rho_s d^2}{\rho_f \nu_f} \frac{1}{a_E c^2 + b_E Re_p}, \tag{21}$$

where $a_E$ and $b_E$ are the model parameters. It is found that $a_E$ varies from 780 to 1500 or more and $b_E$ varies from 1.8 to 3.6 or more [6, 34]. Eq. (21) is referred as as "EF" model (i.e., Engelund and Fredsøe model) hereafter.

## 3. Numerical scheme

This study uses OpenFOAM [21] to solve the governing equations and closures presented in Section 2. The main challenges of solving these equations include (1) how to compute $p_f$; (2) how to avoid the numerical instability caused by high sediment concentration; and (3) how to capture the water-air interface. The first and second challenges also exist in other two-phase flow simulations. Lee et al. [19] combined the "PIMPLE" scheme to solve the equations for the fluid phase [21] and the predicted-corrected scheme to solve the sediment phase [35]. The PIMPLE scheme is a combination of two famous schemes that adjust fluid pressure to keep mass balance: the pressure implicit with splitting of operator (PISO) scheme and the semi-implicit method for pressure-linked equations (SIMPLE) scheme [36]. In the predicted-corrected scheme for the sediment phase [35], the discrete mass-balance equation for the sediment phase [Eq.(3)] becomes an advection-diffusion equation instead of an advection equation. The diffusion behavior subdues the fluctuation in concentration and helps improve the numerical stability when the concentration is high.

Combining Eqs. (3), (4) and (5) gives

$$\nabla \cdot [(1-c)\mathbf{u}^f + c\mathbf{u}^s] = 0. \tag{22}$$

Therefore, the governing equations for the solid-fluid two phases [Eqs. (3), (6), (7), and (22)] are the same as those used in Lee et al. [19]. In the following, we will show how to modify the numerical scheme in Ref. [19] to capture the water-air interface in the presence of the sediment phase.

We first derive the equation governing $s$. From the mass-balance equations [Eqs. (3), (4), and (22)], we obtain

$$\frac{\partial s}{\partial t} + \nabla \cdot \left[s\mathbf{u}^f\right] - s\nabla \cdot \mathbf{u}^f = 0. \tag{23}$$

If the sediment phase is absent, Eq. (22) yields $\nabla \cdot \mathbf{u}^f = 0$, and thus the third term in Eq. (23) disappears, resulting in the classic equation for $s$ used in the VOF method for liquid-gas two-phase flows [26]. Solving Eq. (23) directly causes too much diffusion near the water-air interface. To avoid this, an extra term is included in Eq. (23) to artificially compress the water-air interface [26]. With this extra term, Eq. (23) becomes

$$\frac{\partial s}{\partial t} + \nabla \cdot \left[s\mathbf{u}^f\right] - s\nabla \cdot \mathbf{u}^f + \nabla \cdot [s(1-s)\mathbf{u}^r)] = 0, \tag{24}$$

where $\mathbf{u}^r$ is the velocity field to compress the water-air interface (for details about $\mathbf{u}^r$, the reader is referred to Ref. [26]).

OpenFOAM provides a multi-dimensional universal limiter with explicit solution (MULES) [21] for solving Eq. (24) with guaranteed boundedness of $s$ ($0 \leq s \leq 1$). The numerical procedure to solve the equations in Sections 2 and 3 is summarized below:

1. Solving Eq. (24) for $s$;
2. Calculating $\rho_f$ and $\nu_f$ according to Eqs. (1) and (2), respectively;
3. Computing $\mathbf{u}^f$, $\mathbf{u}^s$, $p_f$, $c$, $k$, and $\epsilon$ using the scheme proposed by Lee et al. [19]. An inner loop and an outer loop are needed: the inner loop repeats $n_i$ times to correct $p_f$; the outer loop repeats $n_o$ times to compute $\mathbf{u}^f$, $\mathbf{u}^s$, $p_f$, $c$, $k$ and $\epsilon$.

Bakhtyar et al. [23] developed a three-phase model with the capability of capturing the water-air interface. Following the study of Hirt [25] on simulating free surface flows, Bakhtyar et al. [23] solved the following equation for $s$

$$\frac{\partial s}{\partial t} + \mathbf{u}^f \cdot \nabla s = 0 \tag{25}$$

in order to track the water-air interface. Eq. (25) is mathematically identical to Eq. (23), except that Eq. (23) is written in its conservation form required by MULES. Their numerical scheme differs from ours in that their scheme requires the bed location to be specified during the computation, preventing their model from simulating avalanche.

## 4. Application to sediment transport in open channel flow

The present model is applied to simulate sediment transport in open channel using the RZ and EF models for $\tau_p$. The purpose of this section was to compare the two models for $\tau_p$ and understand the sensitivity of our three-phase model to uncertainties in two model parameters used in the EF model for $\tau_p$. In our simulations, an uniform 1D vertical mesh was established within the domain with a height of 0.25 m, and the initially static sediment layer was set to occupy the lower portion of the domain with $c = 0.6031$. The initial thickness of the sand layer was set to 0.0525 m. Sand with a diameter of $d = 0.25$ mm and a density of $\rho_s = 2600$ kg/m$^3$ was used in the simulations.

The open-channel flow driven by gravity is assumed to be uniform, and thus a periodic boundary condition can be applied in the direction of the flow and the slip condition on the top boundary. A grid size of $0.625d$ was used. A convergence test performed with a smaller grid size of $0.31d$ showed that the discrepancies between the two meshes were within 3 %. Ten key model parameters used in this study are presented in Table 1, and other model parameters are the same as those used in the previous study of Lee et. al. [19]. The main differences in the model parameters used here and in Ref. [19] are the values of $1/\sigma_c$ and $C_{\epsilon 3}$; the values of these two parameters used here are $1/\sigma_c = 0.6$ and $C_{\epsilon 3} = 0.6$, which were determined based on the simulation results in the next section for the local scour induced by a submerged wall jet issued from a sluice gate.

Fig. 1 shows the dimensionless sediment transport rate $q^*$ versus the Shields parameter $\theta$: $q^* = q/d\sqrt{(\rho_s/\rho_f - 1)gd}$ with $q$ being the dimensional sediment transport rate and $\theta = \tau_b/g(\rho_s - \rho_f)d$ with $\tau_b$ being the bed shear stress. The results computed using both the EF and RZ models are

Table 1: Key model parameters used to produce the results in Fig. 1

| $a$ | $b$ | $I_o$ | $\eta_1$ | $\eta_2$ | $c_c$ | $1/\sigma_c$ | $C_{\epsilon 3}$ | $a_E$ | $b_E$ |
|---|---|---|---|---|---|---|---|---|---|
| 0.11 | 1 | 0.1 | 0.55 | 0.82 | 0.62 | 0.6 | 0.6 | 1000 | 3.6 |

presented in Fig. 1. As suggested by Hsu et al. [14], the near-bed region with $c \geq 0.08$ is regarded as the bed-load layer. The formulas of Meyer-Peter and Müller (MPM) [37] , Hanes [38] and Ribberink [39] are also included in Fig. 1 for comparison. We remark that the formula of Meyer-Peter and Müller [37] is based on the flume experiments for $\theta < 0.2$, the formula of Ribberink [39] is based on the laboratory experiments for $0.07 < \theta < 7$, and the formula of Hanes [38] is based on Bagnold's empirical relationship of strain rate and stress for granular flows [12].

Generally speaking, the total and bed load sediment transport rates given by both the EF and RZ models are similar. For larger values of $\theta$ the total-load and bed-load transport rates given by both models are generally over-estimated compared with the formulas of MPM and Hanes, but close to the formula of Ribberink. For smaller values of $\theta$, the computed sediment transport rate results are closer to the formula of Hanes, but under-estimated compared with the formulas of MPM and Ribberink. It is worth noticing that the bed-load transport rate given by the RZ model at $\theta = 0.1$ is less than $10^{-3}$, indicating the sediment transport is almost all due to the suspended load. However, we should expect a bed-load dominated transport for low $\theta$. Therefore, the EF model will be adopted in the next section to simulate the scouring process downstream of a sluice gate.

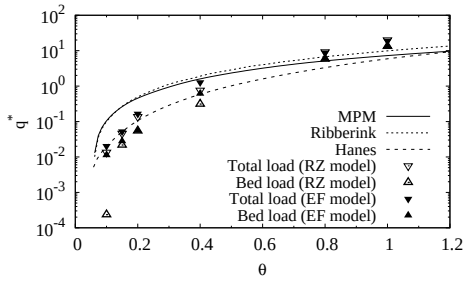


Fig. 1: Sediment transport rates at different values of $\theta$ for open channel flows.

A sensitivity analysis has been performed to determine the sensitivity of the EF model for particle response time to possible uncertainties in the two model parameters: $a_E$ and $b_E$. Changes in the total-load transport rate $q$ was examined in the sensitivity analysis by changing one parameter at a time within a given range with the other parameter being fixed. Three values of $a_E$ were examined: 760, 1000 and 1500, which correspond to spherical particles, rounded sand grains, and irregular angular grains, respectively [6]. The parameter $b_E$ varied between 1.8 and 3.6. We use the total-load transport rate obtained with $a_E = 1000$ and $b_E = 3.6$ are the reference values. When

$0.1 < \theta < 0.4$, the use of $a_E$=760 reduced $q$ by 4%, but the use of $a_E$=1500 increased $q$ by 14%; reducing $b_E$ = from 3.6 to 1.8 introduced a change in $q$ by about 10%.

In the next section, we will use $a_E = 1000$ and $b_E = 3.6$ to simulate the local scour caused by a submerged wall jet issued from a sluice gate. The error in the quantities related to sediment transport is expected to be about 10% due to the uncertainties in $a_E$ and $b_E$.

## 5. Application to the development of local scour downstream of a sluice gate

We now apply the three-phase model to study the local scour downstream of a rigid apron caused by a submerged horizontal wall jet issued from a sluice gate, as shown in Fig. 2. Local scour occurs when the Shields parameter exceeds the critical Shields parameter for sediment initiation. A scour hole forms downstream of the apron and a sand dune forms downstream of the scour hole. Many studies have been devoted to this classical problem experimentally to understand the equilibrium scour depth, the development of scour hole, and the rate of sediment removal [22, 40, 41, 42, 43, 44, 45, 46]. The local scour has been found to be affected by following factors: the particle densimetric Froude number $V/\sqrt{gd(\rho_s/\rho_f - 1)}$ with $V$ being the jet velocity, the jet Froude number $V/\sqrt{gB_o}$ with $B_o$ = sluice gate opening, apron length, tailwater level, and the startup conditions [47]. Some theoretical and numerical studies have also been devoted to modeling the local scour downstream of a rigid apron under submerged wall jets. For example, Hassan and Narayanan [40] proposed a simple semi-empirical theory to predict the time rate of scouring process based on the velocity in the scour hole; Liu and Garcia [4] and Hoffmans and Booij [48] solved the Reynolds-averaged Naiver-Stokes equations for the fluid phase and the Exner equation for bed evolution with empirical models for sediment transport rates. However these existing numerical models did not take into consideration the turbulence modulation and the particle-particle interactions. Three-phase simulations of the local scour due to a submerged wall jet issued from a sluice gate have not been reported in the literature. In this section, we apply our three-phase model to reproduce the experimental results of Run 2 in the study of Chatterjee et al. [42], which reached the equilibrium within 30 minutes (the shortest of all available experiments).

### *5.1. Numerical setups*

Fig. 2 shows the numerical setup, which is the same as the experimental setup used in Ref. [42] except for the reservoir. A two-dimensional computational domain without reservoir is used in the simulation in order to reduce the computational load. Referring to Fig. 2, the sluice gate opening $B_o$ is 2 cm; the length of apron $L_{AP}$ is 0.66 m; the sediment reservoir length $L_s$ is 2.1 m; the overflow weir has a height of 0.239 m; the upstream inflow discharge rate at the sluice opening is 0.204 $m^2/s$, which translates into an average horizontal flow velocity $V = 1.02$ m/s under the sluice

gate; quartz sand with $\rho_s = 2650$ kg/m$^3$ and $d = 0.76$ mm is placed in the sediment reservoir, with its top surface being on the same level as the top surface of the apron. We remark that Chatterjee et al. [42] reported $V = 1.56$ m/s (which was measured by a micropitot tube in the experiment) and $\Delta h$=11.8 cm ($\Delta h$ is the difference between the water level in the reservoir and in the test section). However, the contraction coefficient obtained using the reported values of $V$ and $\Delta h$ exceeds one, which we believe is unreasonable. Therefore, $V = 1.02$ m/s, which is consistent with the discharge rate reported in Chatterjee et al. [42], will be adopted in the simulations presented in the rest of this paper.

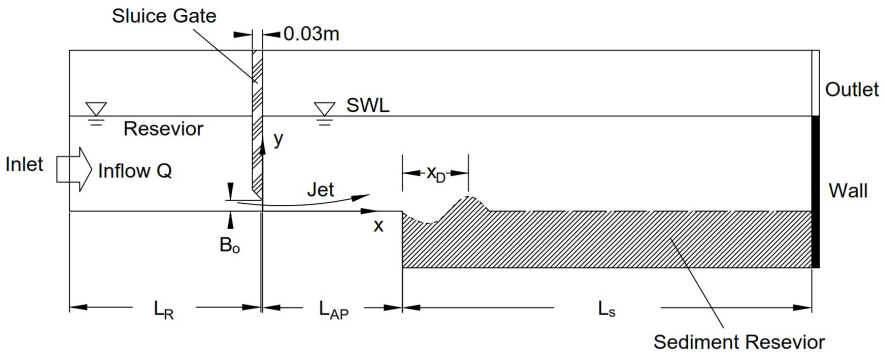


Fig. 2: A sketch of the adapted experimental setup. The water levels in the figure correspond to the initial condition used in the simulation.

For the fluid phase (including liquid and gas), a wall-function boundary condition for smooth wall is imposed on all rigid boundaries. The mean velocity at the sluice gate opening is prescribed according to the given discharge rate. The fluid pressure is set to zero at the upper and outlet boundaries, but the fluid pressure is set to have a zero gradient on other boundaries. For the sediment phase, a no-slip boundary condition is implemented on all rigid boundaries. For both the fluid and sediment phases, the velocity gradient is set to zero at the upper boundary and above the weir. The gradients of saturation $s$ and sediment concentration $c$ are set to zero on all boundaries except at the inlet boundary where $s = 1$ and $c = 0$ are used. Since Chatterjee et al. [42] did not report the detailed startup conditions used in their experiment, we assume here that the initial water depth is 0.239 m and impose a ramping function on the mean velocity of the flow at the sluice gate opening. For details of this ramping function, the reader is referred to Appendix A. For the sediment concentration in the sediment reservoir, an initial value of $c = 0.6018$ is used.

Values for the key model parameters listed in Table 1 were used in the simulations and the friction coefficient $\eta_1$ in Eq. (13), which is related to the angle of repose, was 0.55 in the simulations.

A non-uniform mesh was used in the simulation. The interface between the sediment and fluid requires special treatment in terms of mesh size in order to accurately capture the interfacial mo-

mentum transfer; therefore, the finest mesh with a vertical mesh resolution of $2d$ was used in the vicinity of the sediment-fluid interface. This fine mesh covers the dynamic sediment-fluid interface during the entire scour process. At locations away from the sediment-fluid interface or locations where the scouring is predicted to be negligible (for example, further downstream the sand dune), the mesh sizes with a vertical resolution ranging from 3 mm to 5 mm were used. The aspect ratio of the mesh outside the wall jet region was less than 3.0. Since in the wall jet, horizontal velocity is significantly larger than the vertical velocity, the aspect ratio used in the wall jet region was less than 5.0. A snapshot of the mesh configuration near the downstream edge of the rigid apron and the upstream of sediment reservoir is shown in Fig. B.2 in Appendix B, where the reader can find more details about the mesh setup. A grid-dependence test has been carried out, and the meshes with identical layout but a grid size 25% smaller (finer mesh) or 25% larger (coarser mesh) than the current mesh were used in the test. Compared to the current mesh, at $t = 300s$, the coarser mesh over-predicted the height of the sand dune by 10%, the peak location by 1.5% and under-predicted the scour depth by about 2.6%; the finer mesh under-predicted the height of the sand dune by less than 8% and the scour depth by less than 0.3%, the peak location is over-predicted by 0.6%.

OpenFOAM provides a set of built-in numerical schemes to discretize respective fields, which were used to discretize fields in this numerical work. A Crank-Nicolson scheme with an off-centering coefficient of 0.5 was used for time discretization. For most of the other operators, Gaussian or bounded Gaussian with limiter was used as the discretization scheme. During the initial stage of the simulation, the concentration of the sediment phase changes slightly from the preset value to reach a stable packing status due to elastic effect; during this initial stage a smaller time step was used to ensure the numerical stability. The time step is controlled automatically by the Courant-Friedrichs-Lewy condition with the Courant number $< 0.1$ during the initial sediment settling stage; after $t$=30 s the time step is controlled by Courant number $< 0.3$. A 720-second of physical time takes 3 days on two computation nodes each with two central processing units (Intel Xeon E5-2670), connected using a 40 Gbps infiniband high speed network.

### *5.2. Results and discussion*

Main results to be presented and discussed in this section include: simulated flow field and bed-profile evolution, sediment avalanche, and a sensitivity analysis.

#### *5.2.1. Bed profile and its key characteristics*

Detailed comparisons between the computed scour profiles and those measured [42] at $t = 60, 180, 300, 480,$ 720, 1200 and 1800 s are shown in Fig. 3, where the distribution of sediment concentration is also included. In these figures, the bed profile was determined by the contour line of $c = 0.5$. The water-air interface is also shown in the figures, and the water surface set-down

induced by the submerged wall jet can be noticed in the figures. Under the action of the jet flow, a scour hole develops in the initially flat sand bed downstream of the rigid apron and a sand dune forms downstream of the scour hole. The on-set of sediment scouring is rapid during the initial period, but gradually slows down. As the scour hole develops, its trough location shifts downstream, and the depth and width of the scour hole and the height of the sand dune continue to increase. Further downstream of the sand dune, the sand bed remains mostly unchanged. The general agreement between the simulated and measured bed profiles is satisfactory except for some minor discrepancies between the simulated and measured sand dune profiles after $t = 1200$ s. During the entire process shown in Fig. 3, it can be observed that the extent to which the suspended sediment can reach is more or less the same, which is around $x = 1.2$ m; this appears to be correlated to the final peak location of the sand dune. With the downstream migration of the sand dune, the size of the region where the suspended sand has a concentration larger than 0.0001 is reducing. Theoretically speaking, the final equilibrium is reached when the net sediment transport rate is zero everywhere along the bed profile.

The simulated horizontal location of the sand dune peak, the maximum accretion height, and the depth of the scour hole are shown in Fig. 4, where the experimental data [42] are also included for comparison. The simulated maximum scour depths also agree well with the experimental measurements. Generally speaking, the simulated peak locations of the sand dune $x_D$ agree well with experimental observations except for slight over-estimations when $t > 1200$ s. The maximum accretion heights are slightly under-predicted in general; possible factors that may have contributed to these discrepancies will be discussed later in Section 5.2.5.

*5.2.2. Flow fields of the fluid and sediment phases*

Fig. 5 shows the streamlines and velocity magnitude of the entire flow field taken at $t = 300$, 1200 and 1800 s, including both the liquid phase and the gas phase. Three vortex flow patterns can be observers in the flow field. The formation of these vortex flow patterns is due to flow separation, which itself is caused by the negative pressure gradient near a curved boundary. Flow separation occurs at a point where the shear stress is zero. Therefore, the presence of a vortex flow pattern in a region weakens the flow there.

A very large counter-clockwise vortex can be observed above the jet flow downstream of the sluice gate, and this vortex flow pattern resembles to the one generated by a submerged jet issued from a sluice gate reported in Gumus et al. [49]. While the jet flow passes underneath this large vortex, the jet cross-section gradually increases (see also Fig.5). A small clockwise vortex near the edge of the rigid apron can also be observed, which is consistent with the recirculation pattern observed in the laboratory experiment of Hoffmans and Booij [48]; the small vortex also yields a small scour hole,

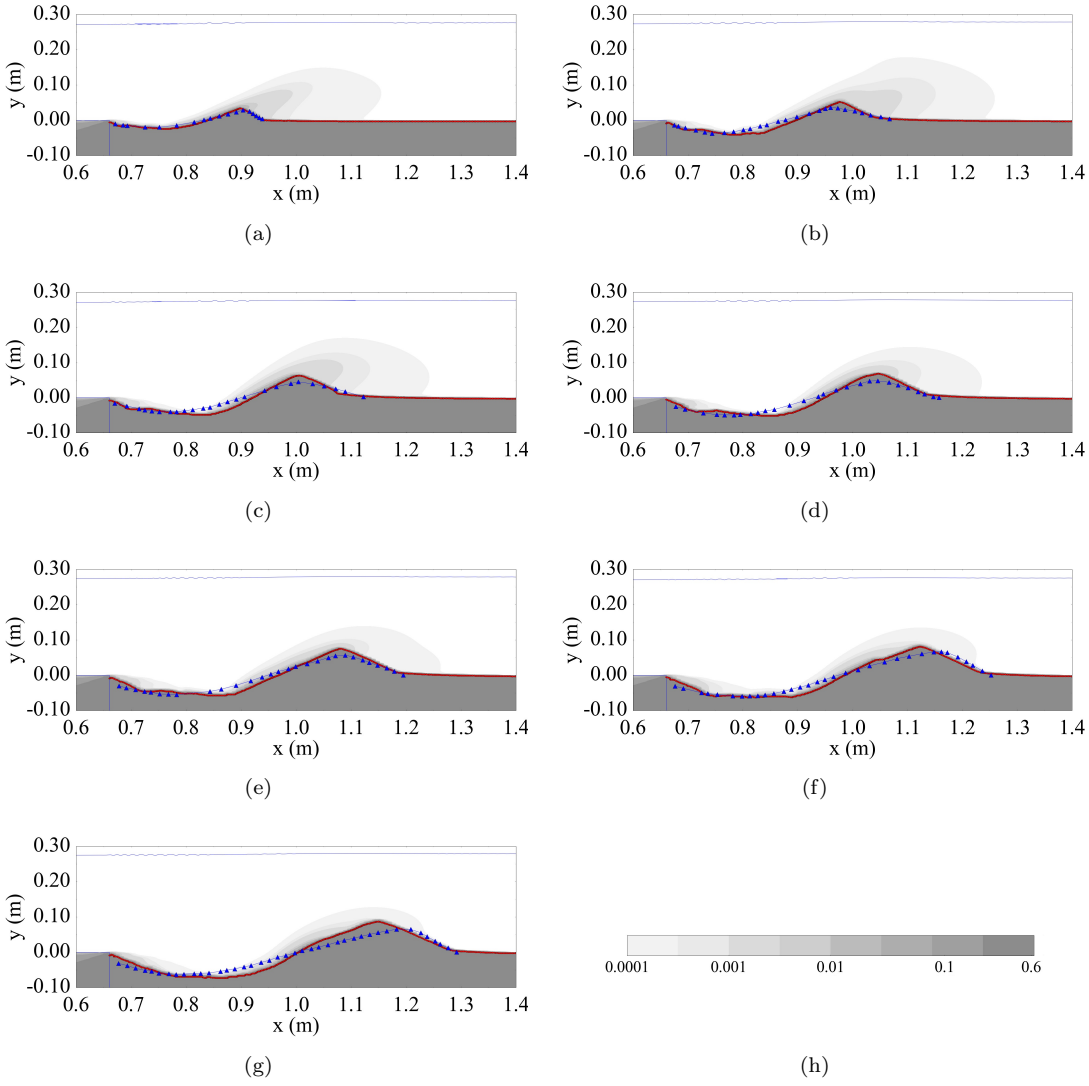


Fig. 3: The scouring profiles (blue triangles: experimental, red lines: simulated by using the three-phase model) and concentration distributions (grayscale contour) at seven time instants: (a):$t = 60$ s; (b):$t = 180$ s; (c): $t = 300$ s; (d): $t = 480$ s; (e): $t = 720$ s; (f): $t = 1200$ s; and (g): $t = 1800$ s. The concentration color bar is shown in (h).

which grows and migrates downstream with time and finally merges into the main scour profile (see also Figs. 5 and 6). As shown in Fig. 5, another medium-sized but weak clockwise vortex in the lee side of the sand dune exists; with the development of the sand dune, this vortex reduces in both size and strength. The presence of the vortex flow pattern in the lee side of the sand dune helps to deposit sand in the region, as shown in Fig. 6 for the flow field of the sediment phase.

Fig. 6 shows the snapshots of sediment-phase velocity fields taken at four time instants: $t = 60, 300, 720$ and 1800 s. In the scour hole, the sediment is mobilized by the jet flow and transported uphill. Before the point of maximum scour depth the sand is transported mainly within a narrow

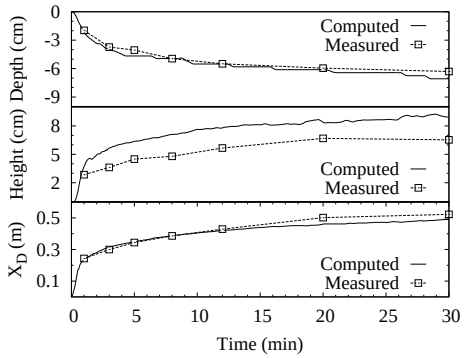


Fig. 4: Evolutions of the peak location $X_D$, peak height and scour depth.

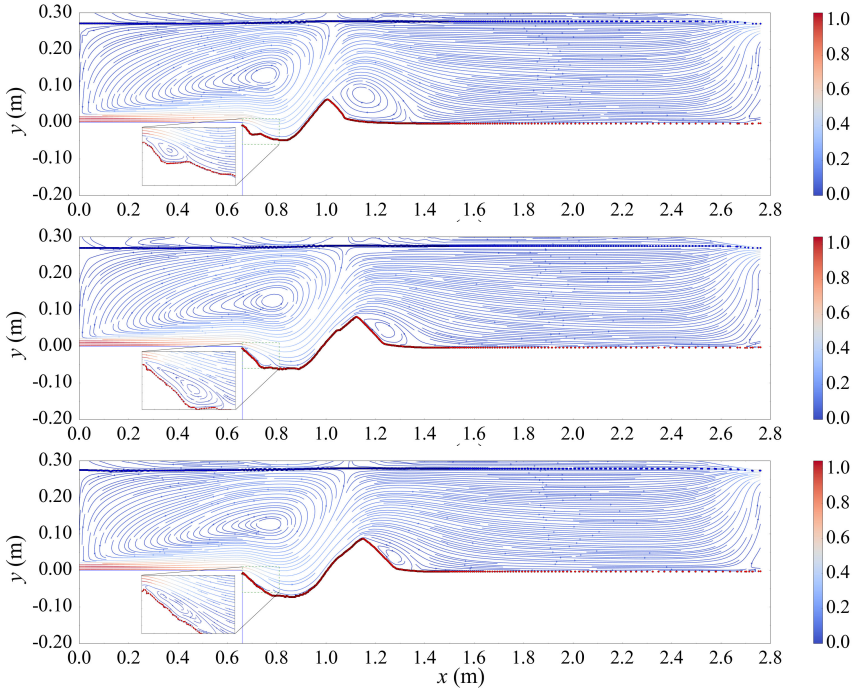


Fig. 5: The computed flow fields for the fluid phase at three time instants: $t = 300$ s (top), $t = 1200$ s (middle) and $t = 1800$ s (bottom). The lines are streamlines and the color bar indicates the magnitude of the fluid-phase velocity. The unit of the velocity is m/s.

region adjacent to the movable bed. Between the point of maximum depth and the dune peak, it appears that both the bed-load and suspended-load transport the sand. After the mobilized sediment particles past the dune peak, they are transported mainly by the sedimentation process because of the low velocity associated with the clockwise vortex behind the sand dune. With the development of scour hole, the size of the region in the lee side of the sand dune where sand moves in suspension reduces in size, making the migration and growth of the sand dune slower.

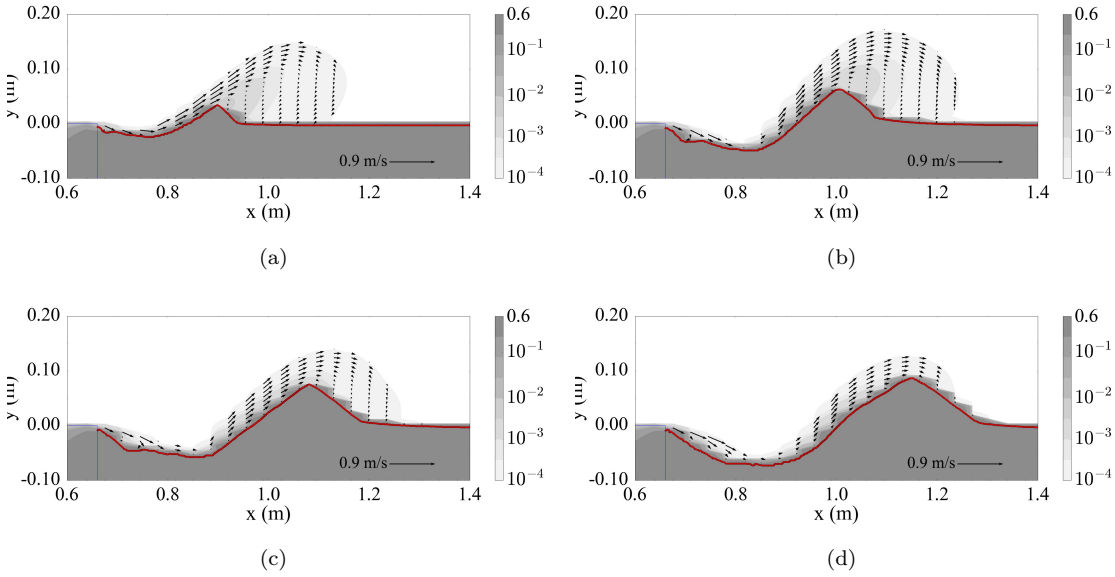


Fig. 6: The computed velocity fields of the sediment phase at four time instants. (a): $t = 60$ s; (b): $t = 300$ s; (c): $t = 720$ s; and (d): $t = 1800$ s.

### *5.2.3. Sediment avalanche*

In their experimental study of effect of grain size on the dynamics of local scour downstream of a sluice gate, Balachandar et al. [22] and Kells et al. [50] observed sediment avalanche, and concluded that reducing the discharge or increasing either the grain size or the tailwater depth reduces the tendency of sediment avalanche. Our simulation also clearly shows the occurrence of multiple sediment avalanching events. As an example, Fig. 7 shows a series of snapshots of back-face profile of the sand dune, capturing an avalanching event occurred between $t = 109.5$ and 111 s. A lump of sediment first moves down the slope against the flow from $t$=109.0 s to 111.0 s, and then moves up the slope with the flow from $t$=111.0 s to 112.0 s. The simulated avalenching event is in consistent with the collapse of sand mass in an erodible sand bed observed in the experiment of Balachandar et al. [22]. The slope of deposited sand on the back face of the sand dune may exceed the angle of repose if there is enough bed shear stress from the flow above to "hold" the sand slope in place. However, when the slope gets so steep that the bed shear stress can no longer balance out the excessive downward gravitational force, avalanching collapse of sand mass may occur locally. After the avalanche, the local flow field is altered and the local bed shear stress is increased, facilitating the forward transport of the sand on the back face until a new balance is reached between the shear stress and the gravitational force.

Our simulation shows that the migration and growth of the sand dune are closely related to the sediment avalanching events. Even though our simulation also shows avalanching events on the

slope close to the apron, these events are not as significant as those on the back side of the sand dune. We remark that avalenching events cannot be captured by traditional one-phase models or two-phase models with one-way coupling between the fluid and sediment phases.

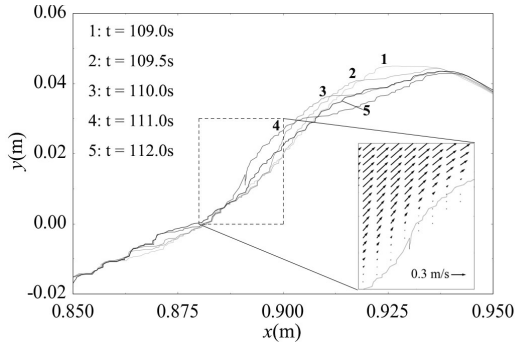


Fig. 7: A series of simulated bed profiles showing a typical avalanching process on the back face of the sand dune.

*5.2.4. Sensitivity analysis*

Lee et al. [19] suggested that $\sigma_c$ and $C_{\epsilon 3}$ should be the two most important parameters affecting the scour underneath a pipeline. The parameter $\sigma_c$ defines the ratio between the turbulent diffusion of the carrier phase and the diffusion of sediment particles. The parameter $C_{\epsilon 3}$ is related to the turbulence modulation due to the presence of particles in the $k-\epsilon$ equations. A sensitivity analysis was performed to determine the sensitivity of the location of the sand dune to these two parameters. It is unlikely that the diffusion of sediment phase can be larger than the diffusion of the carrier phase; therefore, $1/\sigma_c$ would reasonably have a maximum value of 1.0. Based on this rationale, $1/\sigma_c$ in this sensitivity test varied from 0.4 to 1.0. The value of $C_{\epsilon 3}$ varied from 0.5 to 1.2. Previous studies [19, 14] suggested that the typical value of $C_{\epsilon 3}$ should be around 1. This sensitivity tests used $1/\sigma_c$=0.6 and $C_{\epsilon 3}$ =0.6 as the reference values. Fig. 8 summarizes the sensitivity test results. The location of the sand dune at four representative time instants was used to evaluate the sensitivity of the three-phase model to $\sigma_c$ and $C_{\epsilon 3}$. Keeping $C_{\epsilon 3}$ =0.6 but varying $1/\sigma_c$ in the range of 0.4 and 1.0 only causes $X_D$ to have a change less than 11% compared to the reference scenario ($1/\sigma_c = 0.6$); keeping $1/\sigma_c$=0.6 but varying $C_{\epsilon 3}$ in the range of 0.4 and 1.2 only causes $X_D$ to have a change less than 8% compared to the reference scenario ($C_{\epsilon 3}$ =0.6). It is concluded that $x_D$ is not very sensitive to both $1/\sigma_c$ and $C_{\epsilon 3}$ within the tested ranges.

*5.2.5. Discussion*

The minor discrepancies between the simulated and measured key characteristics of the bed profile may be attributed to several factors, including the use of constant $\sigma_c$ and $C_{\epsilon 3}$ obtained through model calibration as discussed below.

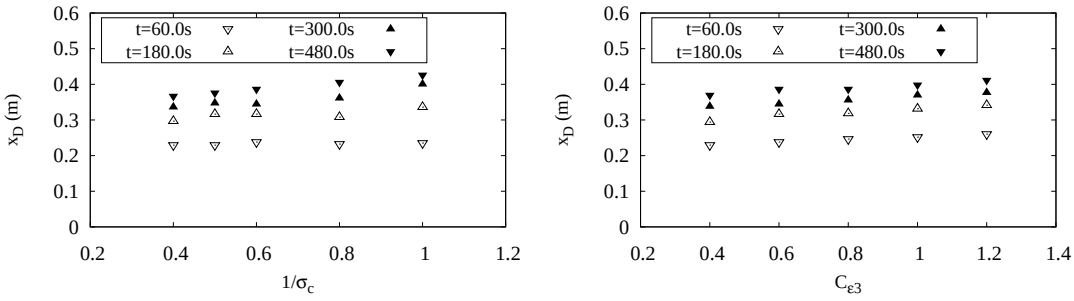


Fig. 8: Results of the sensitivity tests for $1/\sigma_c$ (left) and $C_\epsilon 3$ (right)

In the sensitivity analysis on $1/\sigma_c$ for dilute flows, Lee et al. [51] proposed an expression for $1/\sigma_c$, which depends on two Stokes numbers: $st = \tau_p/\tau_f$ with $\tau_f = 0.165k/\epsilon$ and $st_\eta = \tau_p/\tau_\eta$ with $\tau_\eta$ being the Kolmogorov time scale. Based on their limited results obtained using a direct-numerical-simulation method, Squires and Eaton [52] concluded that the values of $C_{\epsilon 2}$ and $C_{\epsilon 3}$ should be affected by the presence of sediment particles in a particle-laden flow. For $0.6 < C_{\epsilon 3} < 3.84$, in particular, they found that the value of $C_{\epsilon 3}$ decreased with increasing either the concentration of particles or the Stokes number $st$. Because Stokes number $st$ changes with $\theta$, which has both spatial and temporal variations in the present problem, $1/\sigma_c$ and $C_{\epsilon 3}$ should change in space and time as well.

There is a difficulty to use the model for $1/\sigma_c$ proposed by Lee et al. [51]. This is because the flow field in the present problem is much more complex than the open-channel flow studied in Ref. [51] and because the $k - \epsilon$ model in the present three-phase model does not include the sediment-induced turbulence production because of numerical stability issues. Unless an extensive calibration is done, a direct implementation of the expressions for $1/\sigma_c$ summarized in Ref. [51] may not be appropriate. Therefore, this study determined a representative value for $1/\sigma_c$ through model calibration and found that $1/\sigma_c = 0.6$ could give acceptable results. We remark that the ranges of the two Stokes numbers in the present problem also suggest that $1/\sigma_c$ should be between 0.4 and 0.8 according to the conclusions in Ref. [51].

At the present, there is a difficulty to model the temporal and spatial variations of $C_{\epsilon 3}$. Squires and Eaton [52] did not provide enough data to establish a model for $C_{\epsilon 3}$ which can be implemented in our simulations. Again this study determined a representative value for $C_{\epsilon 3}$ through model calibration and found that $C_{\epsilon 3}$=0.6 could give acceptable results. Because the typical Stokes number within the bed-load layer was found to be around 0.5 in the present problem, we should expect a typical value of $C_{\epsilon 3}$ less than 1.0 according to Ref. [52].

It is anticipated that considering both the temporal and spatial variations in $1/\sigma_c$ and $C_{\epsilon 3}$, when

appropriate models for them are available in the future, should reduce the discrepancy between the simulated and measured sand-dune profiles.

## 6. Conclusions

This study presented a rheology-based three-phase model for sediment transport problems with a water-air interface. A modified k-$\epsilon$ turbulence model was employed to compute the fluid-phase shear stresses. A special modification was introduced so that the interface-compression VOF method can track the water-air interface in the presence of the sediment phase. The three-phase model was used to study two problems: sediment transport under 1D open-channel flow condition and local scour induced by a 2D horizontal wall jet issued from a sluice gate. Two models for particle response time were examined in the numerical simulations of the first problem; the Engelund and Fredsøe model for particle response time was found to give better prediction of sediment transport rate for small values of Shields parameter, and thus was used in the three-phase flow simulations of the local scour downstream of a sluice gate. The depth of the scour hole and the location of sand dune predicted by numerical model agreed well with the laboratory experimental results; however, the height of the sand dune at later stage of the scouring process was slightly under-predicted by the present model, which is due mainly to the difficulty in modeling the weak bed shear stress presently. The three-phase model was found to be able to capture sediment avalanche events on the back face of the sand dune.

## Acknowledgement

This study is supported partially by the Ministry of Science and Technology , Taiwan ( MOST 105-2218-E-032-001 ). This work was also supported in part by the National Science Foundation under grant no. CBET-1706938; any opinions, findings and conclusions or recommendations expressed in this material are those of the au- thor(s) and do not necessarily reflect those of the National Science Foundation.

## Appendix A. Numerical implementation of the ramping function

Referring to Fig. A.1, the rate at which the water fills the reservoir is usually constant in the experiment. Until the steady state is reached, the discharge rate $Q_o$ at which the water is discharged through the sluice gate opening into the tank downstream gradually increases. The purpose of using a ramping function is to provide a velocity inlet boundary condition at the sluice gate that can mimic the time-varying behavior of $Q_o$.

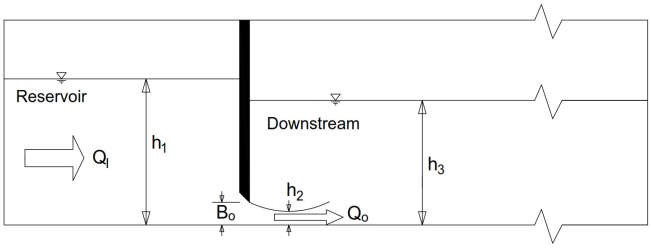


Fig. A.1: A definition sketch for the derivation of the ramping function.

Considering a 2D flume setup with a unit width depicted in Fig. A.1, the continuity of mass requires that:

$$L_R \frac{dh_1}{dt} - (Q_I - Q_o) = 0, \tag{A.1}$$

where $L_R$ is the length of the reservoir, $h_1$ the depth of the water in the reservoir, $h_3$ the depth of the water downstream. We assume that the water level variation downstream of the sluice gate is negligible. Given the water level difference $(h_1 - h_3)$ and the height of the sluice gate opening $B_o$, the sluice gate discharge rate $Q_o$ can be calculated as [53]:

$$Q_o = C_o B_o \sqrt{2g(h_1 - h_3)}, \tag{A.2}$$

where $C_o$ is the discharge coefficient and expressed as :

$$C_o = 0.0297 \frac{B_o}{h_1} + 0.589. \tag{A.3}$$

Substituting Eq. (A.2) into Eq. (A.1) and rearranging yields:

$$L_R \frac{dh_1}{dt} = Q_I - C_o B_o \sqrt{2g(h_1 - h_3)}. \tag{A.4}$$

For given the constant inflow into the reservoir $Q_I$ and the length of the reservoir ($L_R = 1.8$ m in this case), the above equation, combined with Eq. (A.3), can be solved numerically with initial condition of $h_3 = h_1$ to obtain a time-varying discharge rate $Q_o$. Initially $Q_o$ is zero; when the steady state is reached, $Q_o = Q_I$. The time required for the discharge $Q_o$ to reach the steady state is controlled by the reservoir length for given $Q_I$. The discharge velocity of the sluice gate can then be obtained from the discharge rate and the geometry of the sluice gate opening. In the numerical simulation, this time-varying boundary condition can be implemented using groovyBC, an open-source utility for OpenFOAM.

## Appendix B. Mesh layout and Configuration

Fig. B.1 shows a general mesh layout used in the simulation of scouring downstream a submerged horizontal wall jet discussed in Section 5.

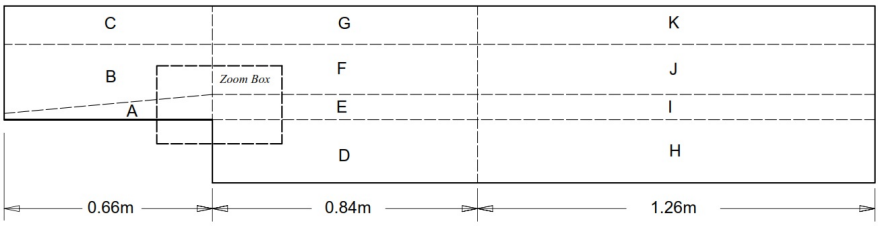


Fig. B.1: The grid layout of the computational domain. The detailed mesh in the zoom box is further shown in Fig. B.2.

The entire computational domain is divided into mesh blocks A∼H. A non-orthogonal mesh is used in blocks A and B to consider the diffusion of the jet flow. In order to properly resolve the jet flow and the sediment scouring, a fine vertical resolution is used at blocks A, E and D, with a vertical mesh size near the mobile sand bed being $2d$ in block E and block D. A graded mesh in the vertical direction is used in block D, so that the vertical mesh is finest near the sand bed interface, and coarser at the bottom of the sand reservoir. The horizontal resolution is finest in blocks D, E, F, G, with a maximum aspect ratio of less than 3.0 in block E. The horizontal resolution in the rest of the blocks is designed so that the aspect ratio does not exceed 5.0. The length of block E is 0.84 m., which is longer than the region with active sediment scouring and deposition. Fig. B.2 shows a snapshot of the mesh configuration in the zoom box indicated in Fig. B.1.

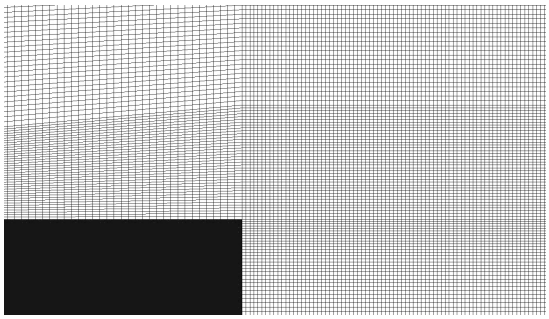

Fig. B.2: The mesh configuration.

## References

[1] B. Sumer, J. Fredsøe, The mechanics of scour in the marine environment, World Scientific Publishing Co Pte Ltd, Singapore, 2002.

[2] B. Brors, Numerical modeling of flow and scour at pipelines, J. Hydraul. Eng. 125 (1999) 511–523.

[3] D. Liang, L. Cheng, F. Li, Numerical modeling of flow and scour below a pipeline in currents:

Part II. Scour simulation, Coast. Eng. 52 (1) (2005) 25–42. doi:10.1016/j.coastaleng.2004.09.002.

[4] X. Liu, M. Garcia, Three-dimensional numerical model with free water surface and mesh deformation for local sediment scour, J. Waterw. Port C-ASCE 134 (4) (2008) 203–217. doi:10.1061/(asce)0733-95ox(2008)134:4(203).

[5] N. Jacobsen, J. Fredsøe, J. Jensen, Formation and development of a breaker bar under regular waves. Part 1: Model description and hydrodynamics, Coast. Eng. 88 (2014) 182–193.

[6] F. Engelund, J. Fredsøe, A sediment transport model for straight alluvial channels, Nord. Hydrol. 7 (5) (1976) 293–306. doi:10.2166/nh.1976.019.

[7] H. Capart, L. Fraccarollo, Transport layer structure in intense bed-load, Geophys. Res. Lett. 38 (20) (2011) L20402. doi:10.1029/2011GL049408.

[8] C. Crowe, T. Troutt, J. Chung, R. Troutt, N. Chung, Numerical models for two-phase turbulent flows, Annu. Rev. Fluid Mech. 28 (1) (1996) 11–43. doi:10.1146/annurev.fl.28.010196.000303.

[9] F. White, Viscous fluid flow, McGraw-Hill, Singapore, 2000.

[10] C. Campbell, Granular material flows-An overview, Powder Technol. 162 (3) (2006) 208–229.

[11] C. Cassar, M. Nicolas, O. Pouliquen, Submarine granular flows down inclined planes, Phys. Fluids 17 (10) (2005) 103301. doi:10.1063/1.2069864.

[12] R. Bagnold, Experiments on a gravity-free dispersion of large solid spheres in a newtonian fluid under shear, Proc. R. Soc. A Math. Phys. Eng. Sci. 225 (1160) (1954) 49–63.

[13] L. Li, M. Sawamoto, Multi-phase model on sediment transport in sheet-flow regime under oscillatory flow, Coast. Eng. Japan 38 (2) (1995) 157–178.

[14] T.-J. Hsu, J. Jenkins, P.-F. Liu, On two-phase sediment transport: sheet flow of massive particles, Proc. R. Soc. A Math. Phys. Eng. Sci. 460 (2048) (2004) 2223–2250. doi:10.1098/rspa.2003.1273.

[15] L. Amoudry, P.-F. Liu, Two-dimensional, two-phase granular sediment transport model with applications to scouring downstream of an apron, Coast. Eng. 56 (7) (2009) 693–702. doi:10.1016/j.coastaleng.2009.01.006.

[16] A. Yeganeh-Bakhtiary, M. Kazeminezhad, A. Etemad-Shahidi, J. Baas, L. Cheng, Euler-Euler two-phase flow simulation of tunnel erosion beneath marine pipelines, Appl. Ocean Res. 33 (2) (2011) 137–146.

[17] T. Revil-Baudard, J. Chauchat, A two-phase model for sheet flow regime based on dense granular flow rheology, J. Geophys. Res-Oceans 118 (2013) 1–16.

[18] F. Chiodi, P. Claudin, B. Andreotti, A two-phase flow model of sediment transport: transition from bedload to suspended load, J. Fluid Mech. 755 (2014) 561–581. arXiv:1401.0807, doi:10.1017/jfm.2014.422.

[19] C.-H. Lee, Y. Low, Y.-M. Chiew, Multi-dimensional rheology-based two-phase model for sediment transport and applications to sheet flow and pipeline scour, Phys. Fluids 28 (2016) 053305. doi:10.1063/1.4948987.

[20] Z. Cheng, T.-J. Hsu, J. C. Calantoni, SedFoam: A multi-dimensional Eulerian two-phase model for sediment transport and its application to momentary bed failure, Coast. Eng. 119 (2017) 32–50. doi:10.1016/j.coastaleng.2016.08.007.

[21] OpenCFD, The Open Source CFD Toolbox: Programmer's Guide (2014).

[22] R. Balachandar, J. Kells, R. Thiessen, Effect of tailwater depth on the dynamics of local scour, Can. J. Civ. Eng. 27 (1) (2000) 138–150. doi:10.1139/l99-061.

[23] R. Bakhtyar, D. A. Barry, A. Yeganeh-Bakhtiary, L. Li, J. Parlange, G. Sander, Numerical simulation of two-phase flow for sediment transport in the inner-surf and swash zones, Adv. Water Resour. 33 (3) (2010) 277–290. doi:10.1016/j.advwatres.2009.12.004.

[24] J. Richardson, W. Zaki, Sedimentation and fluidisation: Part I, Chem. Eng. Res. Des. 32 (1954) S82–S100. doi:10.1016/S0263-8762(97)80006-8.

[25] C. Hirt, Volume of fluid ( VOF ) method for the dynamics of free boundaries, J. Comput. Phys. 225 (1981) 201–225.

[26] H. Rusche, Computational fluid dynamics of dispersed two-phase flows at high phase fractions, Ph.D. thesis (2003).

[27] C. Brennen, Fundamentals of multiphase flows, Cambridge University Press, Cambridge, 2005. arXiv:arXiv:1011.1669v3, doi:10.1007/s11214-006-9083-0.

[28] J. Hinze, Turbulence, Mc Graw Hill, New York, 1959.

[29] M. Trulsson, B. Andreotti, P. Claudin, Transition from the Viscous to Inertial Regime in Dense Suspensions, Phys. Rev. Lett. 109 (11) (2012) 118305. doi:10.1103/PhysRevLett.109.118305.

[30] P. Jop, Y. Forterre, O. Pouliquen, A constitutive law for dense granular flows, Nature 441 (8) (2006) 727–730. doi:10.1038/nature04801.

[31] X. Yin, D. Koch, Hindered settling velocity and microstructure in suspensions of solid spheres with moderate Reynolds numbers, Phys. Fluids 19 (9) (2007) 093302. doi:10.1063/1.2764109.

[32] E. Pitman, L. Le, A two-fluid model for avalanche and debris flows, Phil. Trans. R. Soc. A 363 (1832) (2005) 1573–1601. doi:10.1098/rsta.2005.1596.

[33] N. Chien, Z. Wan, Mechanics of sediment transport, ASCE Publisher, Reston, 1999.

[34] H. Burcharth, O. Andersen, On the one-dimensional steady and unsteady porous flow equations, Coast. Eng. 24 (94) (1995) 233–257.

[35] C.-H. Lee, Z. Huang, Y.-M. Chiew, A three-dimensional continuum model incorporating static and kinetic effects for granular flows with applications to collapse of a two-dimensional granular column, Phys. Fluids 27 (11) (2015) 113303. doi:10.1063/1.4935626.

[36] J. Ferziger, M. Peric, Computational methods for fluid dynamics, Springer, Berlin, 2002.

[37] E. Meyer-Peter, R. Müller, Formulas for bed-load transport, Proc. 2nd Meeting Int. Assoc. Hydraul. Res. (1948) 39–64.

[38] D. Hanes, D. Inman, Experimental evaluation of a dynamic yield criterion for granular fluid flows, J. Geophys. Res. 90 (B5) (1985) 3670–3674. doi:10.1029/JB090iB05p03670.

[39] J. Ribberink, Bed-load transport for steady flows and unsteady oscillatory flows, Coast. Eng. 34 (1) (1998) 59–82.

[40] N. Hassan, R. Narayanan, Local scour downstream of an apron, J. Hydraul. Eng. 111 (11) (1985) 1371–1385. doi:10.1061/(ASCE)0733-9429(1985)111:11(1371).

[41] K. Ali, S. Lim, Local scour caused by submerged wall jets, ICE Proceedings 81 (1986) 607–645.

[42] S. Chatterjee, S. Ghosh, M. Chatterjee, Local scour due to submerged horizontal jet, J. Hydraul. Eng. 120 (8) (1994) 973–992. doi:10.1061/(ASCE)0733-9429(1994)120:8(973).

[43] E. Hopfinger, A. Kurniawan, W. Graf, U. Lemmin, Sediment erosion by Görtler vortices: the scour-hole problem, J. Fluid Mech. 520 (2004) 327–342. doi:10.1017/S0022112004001636.

[44] C. Adduce, G. Sciortino, Scour due to a horizontal turbulent jet: Numerical and experimental investigation, J. Hydraul. Res. 44 (2006) 663–673. doi:10.1080/00221686.2006.9521715.

[45] S. Dey, A. Sarkar, Response of velocity and turbulence in submerged wall jets to abrupt changes from smooth to rough beds and its application to scour downstream of an apron, J. Fluid Mech. 556 (2006) 387–419. doi:10.1017/S0022112006009530.

[46] C. Xie, S. Lim, Effects of jet flipping on local scour downstream of a sluice gate, J. Hydraul. Eng. 141 (4) (2015) 04014088. doi:10.1061/(ASCE)HY.1943-7900.0000983.

[47] M. Aamir, Z. Ahmad, Review of literature on local scour under plane turbulent wall jets, Phys. Fluids 28 (10) (2016) 105102. doi:10.1063/1.4964659.

[48] G. Hoffmans, R. Booij, Two-dimensional mathematical modelling of local-scour holes, J. Hydraul. Res. 31 (5) (1993) 615–634. doi:10.1080/00221689309498775.

[49] V. Gumus, O. Simsek, N. Soydan, M. Akoz, M. Kirkgoz, Numerical modeling of submerged hydraulic jump from a sluice gate, J. Irrig. Drain. Eng. 142 (1) (2016) 04015037. doi:10.1061/(ASCE)IR.1943-4774.0000948.

[50] J. Kells, R. Balachandar, K. Hagel, Effect of grain size on local channel scour below a sluice gate, Can. J. Civ. Eng. 28 (3) (2001) 440–451. doi:10.1139/l01-012.

[51] C.-H. Lee, Z. Huang, Y.-M. Chiew, A multi-scale turbulent dispersion model for dilute flows with suspended sediment, Adv. Water Resour. 79 (2015) 18–34. doi:10.1016/j.advwatres.2015.02.002.

[52] K. Squires, J. Eaton, Effect of selective modification of turbulence on two-equation models for particle-laden turbulence flow, J. Fluid Eng. 116 (4) (1994) 778–784.

[53] N. Rajaratnam, K. Subramanya, Flow equation for the sluice gate, J. Irrig. Drain. Div. 93 (3) (1967) 167–186.